

Single-Phase Metamaterials with Star-Shaped Lattice Structure for an Acoustic Super Lens

Matavalam Hari Prasad¹, Dr. Dhananjay Yadav², Dr. Shaik Shafee³

¹Research Scholar, Dept. of Mechanical Engineering
Sri SatyaSai University of Technology and Medical Sciences,
Sehore Bhopal-Indore Road, Madhya Pradesh, India.

²Research Guide, Dept. of Mechanical Engineering
Sri SatyaSai University of Technology and Medical Sciences,
Sehore Bhopal-Indore Road, Madhya Pradesh, India.

³Research Co-Guide, Director.Dept. of Mechanical Engineering
Kamla Nehru Poly Technic For Women,Hyderabad

Received: 2022 March 15; **Revised:** 2022 April 20; **Accepted:** 2022 May 10

Abstract

We present a single-phase super lens with a low density that can accomplish focusing of sound beyond the diffraction limit. The super lens features a star-shaped lattice structure built of steel those offers numerous resonances to generate anomalous dispersive effects as assessed by negative parameter indices. Our research of the metamaterial band structure reveals that these star-shaped metamaterials exhibit double-negative index features that can mediate these effects for sound in water. Simulations verify the effective focusing of sound by a single-phase solid lens with a spatial resolution of roughly 0.39λ . This superlens has a basic structure, low density and solid nature, which makes it more viable for application in water-based situations. It should be mentioned that the suggested approach may produce a more simple stiffness and mass matrices of the proposed structures, compared with the classic finite element (FE) method. Thereafter, the impacts of the geometrical parameters on the effective constants and band gaps are explored and addressed. Numerical results reveal that the negative Poisson's ratio produces an improved effective Young's modulus of the investigated honeycombs. Furthermore, the band gap occurs at a much lower frequency zone with an unaltered summing band gap width when the Poisson's ratio is in negative values. In general, the work can serve as a guide for the best design of cellular structures.

Keywords: Acoustic, Superlens, Shaped

Introduction

Achieving high-resolution super focusing of sound has been a longstanding challenge. The key to resolving the problem of super-resolution photography is figuring out how to detect evanescent waves; fortunately, this challenge has been significantly lessened in difficulty because to the recent invention of acoustic metamaterials. In most cases, the development of sonic metamaterials involves the use of subwavelength-scale resonant units, which are built in a complicated manner in order to achieve unusual physical features such as negative moduli and a negative mass density. Because of these features, it is possible to concentrate sound to the point where it is able to circumvent the diffraction limit that is imposed by the negative refraction and surface states. On the basis of the super-resolution imaging approach that metamaterials offer, a variety of sonic metamaterials with double-negative, single-negative, or near-zero mass properties have been utilised in the development of a number of super lenses. These super lenses were made possible by the use of a series of super lenses. On the other hand, because of the necessity of constructing resonant components, their structures are typically too intricate and cumbersome. Because of this, the design of superlenses might significantly profit from the development of an innovative, uncomplicated, and lightweight resonant structure. The conventional resonant structure of acoustic metamaterials that is utilised in the construction of a super lens may be classified into the following four types: Helmholtz resonators, three-component resonators, holey-structured metamaterials, and

lumped mass structures are all examples of this type of structure. Helmholtz resonators, which often generate a negative modulus, were initially utilised in the excogitation of a super lens and were built as a planar network to concentrate ultrasound in water. This was the first use of Helmholtz resonators.

After that, a concept for a superlens with a negative effective mass was offered, and it was going to be based on a three-component metamaterial that was going to be composed of rubber-coated gold spheres that were going to be embedded in epoxy¹⁵. In a similar manner, a solid lens with hybrid resonators that focused waves by the application of negative refractive indices was developed. Because of its Fabry-Pérot (FP) resonance, metamaterials with a holey structure that are built from metal plates with drilled holes have been proposed as a means to obtain super-resolution imaging. On the other hand, in order to meet the FP resonant requirement, they will typically demand that the lens thickness be equal to the integer number of the half-wavelength. Because of the negative properties they possess, lumped mass structures, such as perforated slab pillar structures or membrane-based structures³¹, which are typically made up of large pieces of solid material connected by small or soft connectors, can also be designed to perform the function of a super lens if the proper care is taken during the design process. However, all of the aforementioned structures are far too difficult to employ, and they frequently call for the application of a combination of several phases of material. Lattice structures that consist of an interconnected network of elastic beams, such as the Kagome lattice³², the re-

entrant grid³³, and the zigzag lattices^{34,35} structures, are widely used in standalone configurations due to the ease with which they can be constructed and the low density of the configurations they produce. They feature an abundance of bending resonators, which allows them to more readily produce a low-frequency band gap, and they display exceptional

qualities. This is when seen from the perspective of their wave characteristics. However, the majority of recent research have concentrated on the band gap of lattice structures, making them the perfect structures for the construction of new lightweight super-lenses. In this regard, they are the ideal structures.

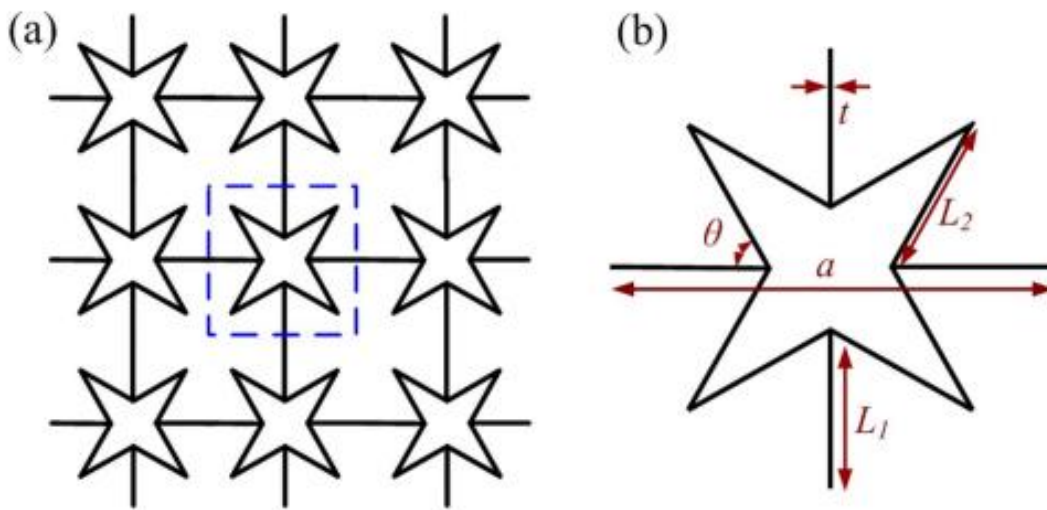


Figure 1: Structural layout (a) and unit cell (b) of the four-point star-shaped structure.

Because of its one-phase composition and lightweight construction, a lattice structure was utilised by us in this article to create a solid super-lens that is suitable for usage in water. The two design requirements were the primary focus of our design approach. The first thing that needed to be determined was how to meet the prerequisites for a single-phase lattice structure that called for negative values. It is not possible to construct a negative density (negative modulus) or a flexural resonance system without the use of a dipole resonance system (lumped mass) (this calls for beams with a sufficiently large slenderness ratio). The second requirement for the solid lens

concentrated on determining how to focus longitudinal sound (in an environment consisting of water) (coexisting with longitudinal and transverse modes). The structure must be capable of undergoing volumetric deformation and strong coupling with sound in water in order for it to function properly. On the basis of the aforementioned principles, it was suggested that the solid super lens should have a lattice structure in the shape of a star. A metamaterial in the shape of a star features a unique re-entrant structure and a square-symmetrical configuration, both of which facilitate volumetric deformation in an easier manner. When the ratio of the beam's

slenderness to its width is sufficiently high, it has the potential to generate a large number of resonances. These resonances may include dipole resonances as well as bending resonances, which can result in abnormal dispersive effects that are associated with the beam's negative parameters. The analysis that is presented below suggests that due to the abundant vibration modes that they possess, single-phase metamaterials with star-shaped structures result in double-negative properties with certain frequency bands and are the ideal structures to construct solid super lenses. These findings are supported by the fact that these structures are presented below.

MICROSTRUCTURAL DESIGN OF THE SINGLE-PHASE HYPERBOLIC EMM WITH ANISOTROPIC MASS DENSITY

As a first physical manifestation of a single-phase EMM plate, the one we provide here is capable of manipulating LR movements in the two primary in-plane directions separately (as seen in Fig. 2), and this is what we present here. The value t represents the thickness of the EMM plate along the z -axis. The single-phase EMM unit cell is suggested to include two decoupled resonators, one in the x -direction and the other in the y -direction. These resonators are in-plane horizontal and in-plane vertical, respectively. Because of this, it is reasonable to anticipate that the EMM will exhibit negative effective mass densities in the two primary directions within certain frequency ranges. The width of the slots is denoted by the letter s , while the in-plane lattice constant of the square unit cell is denoted by the letter a . For the vertical resonator of the unit cell, there are two

horizontal ribs with length r_h and width b_h , and for the horizontal resonator, there is one vertical rib with length r_v and width b_v . The radius of the vertical resonator is denoted by R_1 , while the radius of the horizontal resonator is denoted by R_2 . It is possible to tailor the LR frequencies independently, which leads to anisotropy in the effective mass density because of the design's standout feature, which is that the LR motions of the EMM along the two principal in-plane directions are fully decoupled from one another. This is what makes the design so exceptional. 19,20 The in-plane bending stiffness of the rib beams and their connected masses are what define the LR frequencies of the metamaterial along the two primary directions in the current configuration. Because of the design of the single-phase microstructure, it is very possible to apply the suggested hyperbolic EMM design to thin plate structures using precision manufacturing techniques such as laser cutting or CNC machining. This was made possible by the fact that the single-phase microstructure design was used. The effective material characteristics of the metamaterial shown in Figure 1(a) with two in-plane resonators will be investigated in order to reflect the internal physical wave phenomena as a means of providing a clear illustration of this concept. Calculating the effective material characteristics of the proposed EMM will need the use of the numerical-based effective medium approach due to the complicated microstructure present in the unit cell. The applied local displacement on the border of the EMM unit cell may be represented as u_0 in the finite element model (FE model), where u_0 is a stiff translation and

Eab is the global strain. After that, the effective medium parameters may be derived using numerical analysis by taking into account the boundary responses of the unit cell to the stimulation that is being applied by the elastic waves. Under the assumption of a long wavelength, it is possible to numerically determine the global stress, strain, resultant force, and acceleration of the unit cell by averaging the local values on the exterior border of the unit cell as

$$\Sigma_{\alpha\beta} = \frac{1}{V} \int_{\partial V} \sigma_{\alpha\gamma} x_{\beta} ds_{\gamma}, \quad E_{\alpha\beta} = \frac{1}{2V} \int_{\partial V} (u_{\alpha} ds_{\beta} + u_{\beta} ds_{\alpha})$$

$$F_{\alpha} = \frac{1}{V} \int_{\partial V} \sigma_{\alpha\beta} ds_{\beta}, \quad \ddot{U}_{\alpha} = \frac{1}{V} \int_{\partial V} \ddot{u}_{\alpha} ds,$$

Where Rab, Fa, and U€a are the global stress, resultant force and acceleration, respectively. rab, xa, ua, and u€a are the local

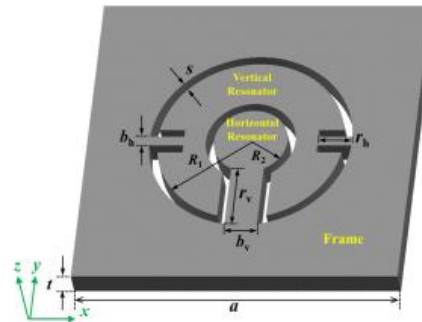


FIG. 2. (Color online) Unit cell design of the proposed single-phase EMM.

Method

Their similar mechanical qualities, but also because of the peculiarities of the pass and stop bands, they have encouraged a variety of investigations of wave propagation. It is particularly fascinating to consider the possibility that periodic honeycombs may prevent the propagation of elastic waves at certain frequency intervals. These frequency intervals are typically referred to as elastic "stop bands," "band gaps," or otherwise "pass bands." This

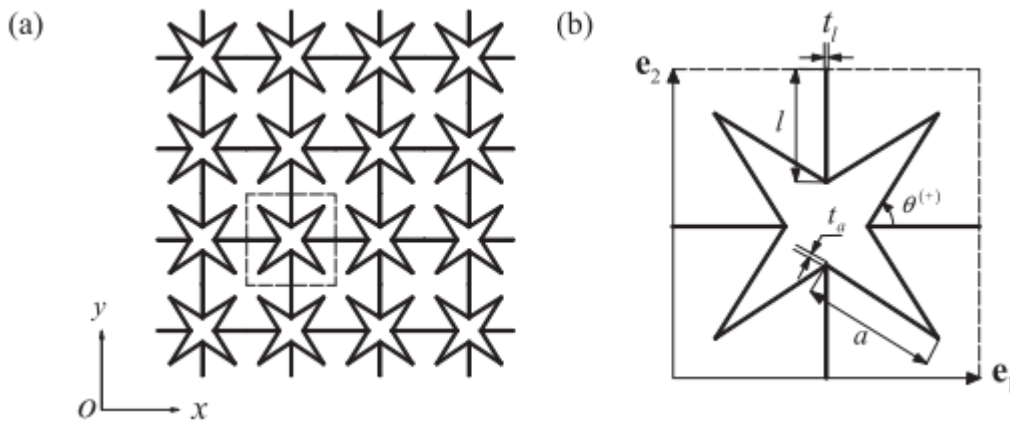


Figure 3. (a) Geometry of a star-shaped honeycomb and (b) the selected primitive unit cell with the basis vectors of the direct lattice ei.

This kind of event has the potential to be utilised fruitfully in a number of essential applications, such as a vibration filter and isolation systems. As a result, there have been a lot of attempts made to modify honeycombs such that they have more acceptable band gap properties. For the purpose of designing periodic cellular structures with optimal band gap properties [25, 26], methodical research that is based on topology optimization processes have been carried out. The method of building a two-dimensional lattice system with predetermined low-frequency stop bands can be accomplished by spreading the mass throughout the connections of the lattice structure, as described in. This is a more broad strategy, and it is not limited to only two dimensions like some other methodologies are. The simulation of the in-plane elastic wave propagation in four typical planar topologies (i.e. hexagonal, Kagome, triangular, and square lattice structures) has been carried out in order to investigate wave band gaps and spatial filtering processes. Additionally, the occurrence of band gaps in various honeycombs as well as their locations have been investigated, with a specific focus on evaluating the functionality of cells exhibiting re-entrant configurations and NPR behaviour.

Recent research has also focused on the study of auxetic chiral lattice structures. The link between Poisson's ratio and stress waves or vibrations has been the subject of research throughout the course of the past several years. It is possible to draw the conclusion that the materials and constructions that have NPR have the potential to give some intriguing and important benefits for the applications of wave

propagation and vibration transmissibility reduction. In spite of the fact that the static and wave propagation properties of a wide variety of honeycombs, such as the traditional topologies and the NPR honeycombs, have been subjected to a great deal of research, to the best of our knowledge, there have been relatively few studies focusing specifically on star-shaped honeycombs. To first attempt to simulate the periodic fiber-reinforced composite with star-shaped encapsulated inclusions, a star-shaped, two-dimensional beamlike cell with re-entrant corners was proposed. According to the findings, the primary factor that determines the apparent Poisson's ratio of a non-convex microstructure is the geometry of the re-entrant corner of the microstructure. Other research focused on the static auxetic behaviour of this form of structure and investigated the possible auxetic behaviour of a 'arrowshaped' unit in star-shaped honeycombs.

According to the findings of these investigations, the comparable mechanical characteristics are mostly determined by the internal angles of the re-entrant corners and the slenderness ratios of the cell wall. Nevertheless, in this previous research, only a small handful of varied geometrical factors were taken into consideration. The static and dynamic behaviours of the star-shaped honeycombs with Poisson's ratios shifting from negative to positive values are deserving of additional investigation in light of this statement. The primary purpose of this article is to broaden the scope of this study. To begin, we carried out an equilibrium analysis so that we could determine the forces that were ultimately exerted on each

cell wall of the unit cell. Following that, we determined the displacements of the unit cell in both the loading direction and the lateral direction by applying the second theorem of Castigliano. Following this, closed form formulas may be derived for determining the effective Young's modulus and Poisson's ratio of star-shaped honeycombs, as described in sections 1 and 2 respectively. Then, Bloch's theorem was presented as the key instrument for analysing wave propagation in honeycombs structured like stars when it was developed. Calculating the dispersion relations of honeycombs required using the dynamic stiffness matrix in conjunction with the W-W method. This was done on the basis of a theorem that was presented before. In comparison to the classic FE approach the primary benefit of the method that was suggested which can be used to construct the stiffness and mass matrices of complicated structures with relative ease is that it can be used to form the matrices. The present investigation is broken up into five pieces, including the Introduction that was described earlier in this paragraph. The arrangement of honeycombs in the shape of stars is discussed in Section 3 along with the derivations of the effective elastic constants for the in-plane direction. In the third portion of this paper, both the finite element model of the basic unit cell and the suggested methodology for analysing wave propagation are discussed. In part 4, the numerical results are detailed, and then in section 5, a conclusion is drawn from all that has been discussed.

In-plane equivalent mechanical properties of starshaped honeycombs

The profile and dimensions of a unit cell

Figure 3 illustrates both the structural architecture of the star-shaped honeycombs as well as the coordinate system that was used (a). After choosing an appropriate primitive unit cell, as illustrated in figure 1(b), one may acquire the full direct lattice by tessellating the unit cell along the basis vectors e . This will result in the formation of the lattice $II =$ Figure 1 demonstrates that honeycombs in the shape of stars are made up of square re-entrant corners with lengths and thicknesses that are equal to one another. These corners are connected by straight ligaments or ribs that have lengths and thicknesses that are also equal to one another. The angle that forms between the neighbouring cell walls with a counterclockwise rotation is represented by the symbol. The dimension of the cell walls in the z direction is designated by the letter b , which is not depicted in figure 3. This is done for the sake of simplicity. It should be noticed that there is a geometrical restriction between these five factors, and that the constraint is a cosine angle greater than a .

Accordingly, the lattice basis vectors can be expressed as

$$e_1 = \left(2 \left(\frac{\sin(\theta - \pi/4)}{\sin(\pi/4)} \cdot a + l \right), 0 \right)^T,$$

$$e_2 = \left(0, 2 \left(\frac{\sin(\theta - \pi/4)}{\sin(\pi/4)} \cdot a + l \right) \right)^T$$

Young's modulus

It is believed that honeycomb structures in the shape of stars are built of isotropic elastic materials that have Young's modulus E and

Poisson's ratio ν . As a result, the shear modulus may be calculated using the formula $G = + E / [2(1 + \nu)]$. For the purpose of an analytical method, the cell walls of the unit cell are modelled as uniformly thin beams that are subjected to linearly elastic deformations. Honeycomb appears to be isotropic because it has a high degree of symmetry in its geometry and morphology. This means that if one applies a uniaxial compressive stress in either the x or y direction to the honeycomb shown in figure 1, the obtained effective Young's modulus and Poisson's ratio both satisfy $E_{12} = E$ and $\nu_{12} = \nu$. This is because the honeycomb has a high degree of symmetry in its geometry and morphology. As a result, the only information required to calculate the independent in-plane effective elastic constants is the value of E_1 and ν_{12} . Meanwhile, the in-plane isotropy requires $G_{12} = E_1 / [2(1 + \nu_{12})]$, we will now focus on the deformation of the primitive unit cell, as seen in figure 1, in order to calculate the in-plane effective elastic constant E_1 of star-shaped honeycombs. This will allow us to determine how much the primitive unit cell deforms (b). When a global in-plane compressive stress of σ_{xx} is applied to the honeycomb in figure 1(a) in the x direction, it is obvious that the deformation of the selected primitive unit cell can be obtained by only one quarter of the unit cell, which includes beams AB, BC, CD, and DE, as shown in figure 2. This is because of the geometrical and loading symmetries (a). The expression for the horizontal force P that is acting at point A of the cell wall AB is as follows:

$$P = \left(\frac{\sin(\theta - \pi/4)}{\sin(\pi/4)} \cdot a + l \right) b \sigma_{xx}$$

It is abundantly clear that the internal forces exerted by beams AB, BC, CD, and DE are functions of the corresponding positions $x_1, x_2, x_3,$ and x_4 that are represented in figure 2. In order to determine the forces that were exerted by the statically indeterminate structure as a result, we carried out an equilibrium analysis. The following is a comprehensive breakdown of how the internal forces of the statically indeterminate structure, which can be seen in figure 2(a), were derived: In this particular investigation, the force technique of a statically indeterminate structure is utilised. The initial structure seen in figure 3(a) becomes equal to a statically determinate structure known as the released structure when redundant constraints are removed. The released structure is subject to loads and redundant forces X_1 , as depicted in figure 3. After determining the value of the fundamental parameter X_1 , it is generally known that a problem that was previously statically indeterminate can be transformed into a problem that was previously statically definite. In accordance with the conformability of deformation, the redundant force X_1 may be reached by resolving equilibrium equations, which is a method that is sometimes referred to as the typical equation of force:

$$\delta_{11} X_1 + \Delta_{1P} = 0 \tag{3}$$

Where δ_{11} represent the displacement along the direction of the redundant force when X_1 is equal to 1 and Δ_{1P} represents the displacement along the direction of the redundant force when P is a horizontal force. In the field of structural

mechanics, the displacements δ_{11} and Δ_{1P} may be calculated using a method called diagram multiplication. This approach is founded on the bending moments of M_1 and M_P , which are depicted in figure 4. Therefore, δ_{11} and Δ_{1P} may be represented by the following:

$$\delta_{11} = \int \frac{\overline{M}_1 \overline{M}_1}{EI} dx = \frac{1}{EI_a} (1 \times a \times 1 + 1 \times a \times 1) = \frac{2a}{EI_a}$$

$$\Delta_{1P} = \int \frac{\overline{M}_1 M_P}{EI} dx = \frac{1}{EI_a} \left(\frac{1}{2} \times Pa \sin \theta \times a \right)$$

$$+ \frac{1}{EI_a} \left(\frac{1}{2} (Pa \sin \theta + Pa (\sin \theta - \cos \theta)) \times a \right)$$

$$= \frac{1}{EI_a} \left(\frac{3}{2} Pa^2 \sin \theta - \frac{1}{2} Pa^2 \cos \theta \right)$$

Substituting equation (4) into equation (3), the redundant force X_1 can be obtained thus,

$$X_1 = -\frac{\Delta_{1P}}{\delta_{11}} = -\frac{3}{4} Pa \sin \theta + \frac{1}{4} Pa \cos \theta$$

The bending moments of the released structure, depicted in figure 3, may be simply calculated along the locations x_1 , x_2 , x_3 , and x_4 when subjected to the horizontal load P and the resultant of the redundant force X_1 .

beam AB: $M_1(0) = 0, M_1(l) = 0 \Rightarrow M_1(x_1) = 0,$

$(0 \leq x_1 \leq l)$

beam BC: $M_2(0) = 0, M_2(a) = \overline{M}_1 X_1 + M_P$

$$= -\frac{3}{4} Pa \sin \theta + \frac{1}{4} Pa \cos \theta,$$

$$\Rightarrow M_2(x_2) = P \sin \theta \cdot x_2$$

$$- \left(\frac{3}{4} Pa \sin \theta - \frac{1}{4} Pa \cos \theta \right),$$

$(0 \leq x_2 \leq a)$

beam CD: $M_3(0) = \overline{M}_1 X_1 + M_P = -\frac{3}{4} Pa \sin \theta$

$$+ \frac{1}{4} Pa \cos \theta + Pa \sin \theta$$

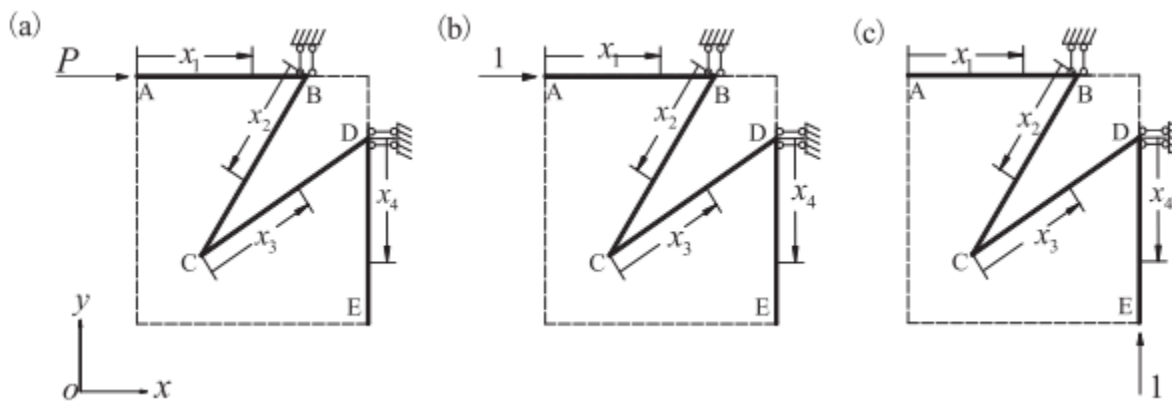


Figure 4. The corresponding representative walls of the linked structure when (a) the horizontal force P is operating at point A, (b) a horizontal unit force is acting at point A, and (c) a vertical unit force is acting at point E.

$$\begin{aligned}
 &= \frac{1}{4}Pa \sin \theta + \frac{1}{4}Pa \cos \theta, \\
 M_3(a) &= \overline{M}_1 X_1 + M_P = -\frac{3}{4}Pa \sin \theta \\
 &\quad + \frac{1}{4}Pa \cos \theta + Pa(\sin \theta - \cos \theta) \\
 &= \frac{1}{4}Pa \sin \theta - \frac{3}{4}Pa \cos \theta, \\
 \Rightarrow M_3(x) &= -P \cos \theta \cdot x_3 \\
 &\quad + \left(\frac{1}{4}Pa \sin \theta + \frac{1}{4}Pa \cos \theta \right), \\
 &\quad (0 \leq x_3 \leq a) \\
 \text{beam DE: } M_4(0) &= 0, \quad M_4(l) = 0 \Rightarrow M_4(x_4) \\
 &= 0, \quad (0 \leq x_4 \leq l)
 \end{aligned}$$

Dispersive analysis of star-shaped honeycombs

Unit cell analysis

The behaviour of a unit cell may be simply explained by applying basic FE processes and the cell's interaction with its neighbours. Additionally, the cell's behaviour can be influenced by the surrounding cells (see figure 5). In order to determine the precise location of the unit cell, the integer pair (n_1, n_2) is first presented. Using the primitive unit cell $(0, 0)$ as a point of reference, the integer pair (n_1, n_2) may identify any other cell that is created by performing n_1 translations along the e_1 direction and n_2 translations along the e_2 direction. The chosen unit cell (n_1, n_2) is modelled here as an assembly of rigidly coupled basic beams. This assembly is then discretized into beam components using the appropriate mesh size in the subsequent analysis to guarantee that the estimated results are accurate, as illustrated in figure 7. (a). Each beam element may be thought of as a two-node element with three degrees of freedom per

node, as illustrated in figure 7; these degrees of freedom include axial displacement, transverse displacement, and rotation in the local coordinate system (b). The Timoshenko assumptions are used in the modelling of bending. In the local coordinate system, the expression for the displacement vector of the beam element with nodes I and j, which is seen in figure 7(b), may be written as

$$\mathbf{u} = \{ \mathbf{u}_i^T, \mathbf{u}_j^T \}^T = \{ u_{xi}, v_{xi}, \theta_{\eta i}, u_{xj}, v_{xj}, \theta_{\eta j} \}^T$$

The elemental mass and stiffness matrices in the local coordinate system may be easily constructed by using the Timoshenko beam model as the basis. These corresponding elemental mass and stiffness matrices should be transformed reciprocally to the forms in the global coordinate system $(xyz,)$ by the application of standard FE procedures. This is accomplished by first utilising the transformation matrix, which is denoted as M_{ge} and K_{ge} (the suffix g denotes the global coordinate system $(xyz,)$). Following this step, the mass matrix M_{ge} and the stiffness matrix K_{ge} are put together to produce the primitive unit cell's mass matrix $K(,)$ $n_1 \times n_1 \times 2$ and its associated stiffness matrix $M(,)$ $n_1 \times n_1 \times 2$.

Bloch's theorem is then introduced to relate the external/boundary displacements $u_e(,)$ $n_1 \times n_1 \times 2$ in the global coordinate system for the wave propagation analysis that is described in the following subsection. The suffix e denotes the external nodes of the cell. Once the stiffness and mass matrices have been obtained the exterior components of the input and output of the displacement vector $u_e(,)$ $n_1 \times n_1 \times 2$ are

designated by the subscripts a and b, respectively. These components are as follows:

$$\mathbf{u}_e^{(n_1, n_2)} = \left\{ \left\{ \mathbf{u}_a^{(n_1, n_2)} \right\}^T, \left\{ \mathbf{u}_b^{(n_1, n_2)} \right\}^T \right\}^T$$

As seen in figure 7(a), the input displacement u_a and output displacement u_b contain two nodal displacements, i.e.

$$\begin{aligned} \mathbf{u}_a^{(n_1, n_2)} &= \left\{ \left\{ \mathbf{u}_1^{(n_1, n_2)} \right\}^T, \left\{ \mathbf{u}_2^{(n_1, n_2)} \right\}^T \right\}^T, \mathbf{u}_b^{(n_1, n_2)} \\ &= \left\{ \left\{ \mathbf{u}_3^{(n_1, n_2)} \right\}^T, \left\{ \mathbf{u}_4^{(n_1, n_2)} \right\}^T \right\}^T \end{aligned}$$

Where u_j ($j = 1, 2, 3, 4$) is termed as the displacement vector of the lattice points in the global coordinate system.

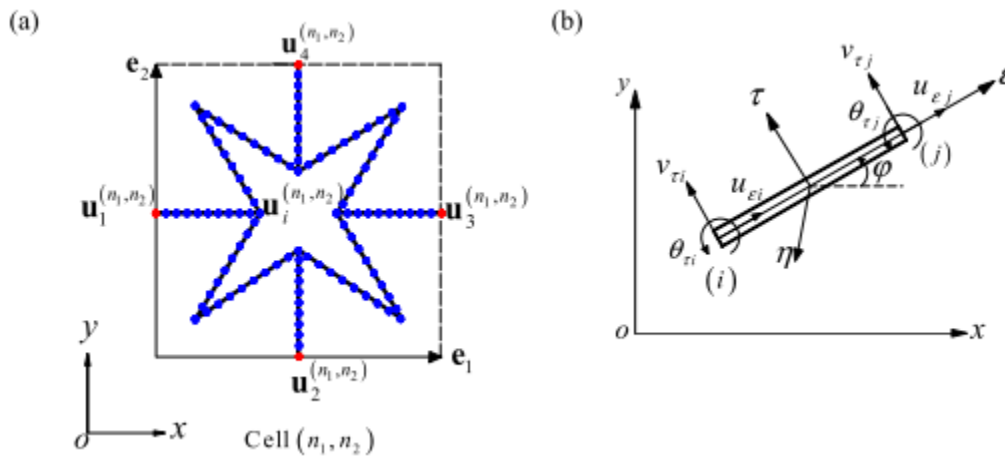


Figure 5. Illustration of (a) the unit cell (n_1, n_2) of a star-shaped honeycomb with its degrees of freedom and (b) a beam element with nodes i and j for FE modeling.

Results and discussion

The numerical application for this section includes the elastic modulus of aluminium, which is Young's modulus $E = 72$ GPa, Poisson's ratio $\nu = 0.3$, and mass density 2700 kg m^{-3} . The length of the basic cell is always the same: 0.05 metres. The effective elastic constants and band gap characteristics of star-shaped honeycombs will be discussed in depth in the following study. The results that are presented here are derived from the Timoshenko beam model rather of the Euler model beam because the Timoshenko beam model is more accurate than the Euler model beam.

Effective elastic constants

In this part, the development of the equivalent mechanical characteristics E^* and ν_{12} is obtained using four different independent parameters, a and l . The results of this subsection are depicted in figure 9. The influence of the cell wall aspect ratio, a/l , on the effective elastic constants is depicted in Figure 9(a), where 0.1 , 0.1 and 70° are used as the parameter values. When the geometrical restriction $a \cos l$ is taken into mind, namely $1 \cos 70$, the aspect ratio varies successively from 0.5 to 2.9 . Figure 9a shows that the normalised Young's modulus E^* declines as the aspect ratio increases, but the effective Poisson's ratio ν_{12}

exhibits the opposite trend. This can be seen by comparing the normalised Young's modulus E^* to the effective Poisson's ratio ν^* . Additionally, when α is less than 1.5 , we discover that there exist quasi linear relations between the effective constants and the aspect ratio. The development of the effective elastic constants versus the slenderness ratio α is depicted in Figure 9(b), where $\alpha = 1, 0.1$ and $\alpha = 10$ are used as independent variables. The normalised Young's modulus E^* grows greater when the slenderness ratio gets larger, especially for larger values of α . This is especially true for larger values of α . On the other hand, the effective Poisson's ratio ν^* will drop if there is a rise in the slenderness ratio α . The influence of the slenderness ratio α on the effective elastic constants is depicted in Figure 9(c), which uses $\alpha = 1, 0.1$ and $\alpha = 10$ as the parameters. At first, it would appear that the normalised Young's modulus E^* rises quickly within a relatively short range of the slenderness ratio $[0.002, 0.03]$, but after that, the growth pace slows down until it reaches $E^* = 0.63 \times 10^3$, and this continues until $E^* = 0.63 \times 10^3$. On the other hand, the effective Poisson's ratio ν^* decreases dramatically in the range of the slenderness ratio $[0.002, 0.03]$ initially, and then the slope decreases until $\nu^* = 0.76 \times 10^{-1}$. Lastly, the effective Poisson's ratio ν^* decreases dramatically in the range of the slenderness ratio $[0.002, 0.03]$. The internal angle varies in the range of $\arccos(\frac{1}{\alpha})$ to 180° when the geometrical constraint $\alpha \cos \theta = 1$ is in place. This allows for greater flexibility in the design of phononic crystal devices and offers the possibility of selecting an internal angle that is better suited to meet a variety of requirements.

For the purpose of illustrating our findings from the numerical investigation of the influence of the internal angles on the effective elastic constants, which is depicted in figure 9(d), we use the values $\alpha = 1, 0.1$ and $\alpha = 10$. The process of evolution.

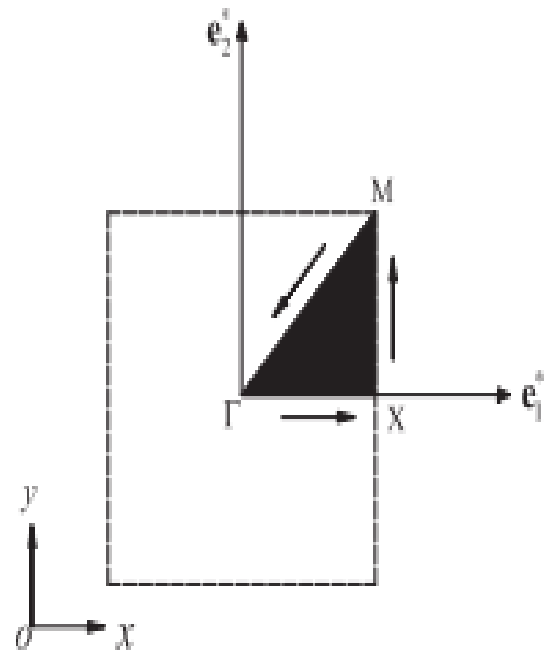


Figure 6. The first Brillouin zone of the honeycomb in the shape of a star, defined by the dashed lines, as well as the irreducible Brillouin zone, which is denoted by the darkened region designated by the letter M. In addition to this, the basis vectors of the reciprocal lattice e_1, e_2 have been shown below.

The values of the effective elastic constants are no longer a monotone function of the internal angle, whereas the extreme values of the effective elastic constants may be attained by setting equal to 135 degrees. When the internal

angle changes within a narrow range, specifically 45 to 90 degrees, the normalised Young's modulus E^* (the Poisson's ratio ν_{12}) undergoes a dramatic decrease (increase), going from $0.95 \cdot 10^{-3}$ (0.97) to $0.39 \cdot 10^{-3}$. This is because the normalised Young's modulus E^* is proportional to the Poisson's ratio ν_{12} (0.59). When the internal angle is increased from 90 to 180 degrees, the development of the normalised Young's modulus, also known as Poisson's ratio, approaches symmetry at an angle of around 135 degrees. For the sake of practical applications, the internal angles can thus be configured to fall anywhere between 45 and 135 degrees. In conclusion, as the values of the four independent factors, a , l , and ν_{12} are raised, the normalised Young's modulus E^* and the Poisson's ratio ν_{12} display opposing trends. To be more specific, when the Poisson's ratio ν_{12} is reduced, the Young's modulus will increase, indicating that the NPR offers an improved effective Young's modulus of star-shaped honeycombs. According to the findings of the research on the orders of magnitude of the effective elastic constants, the effect of the internal angle is more important than the other three factors for determining the effective Poisson's ratio, whereas the length ratio and the slenderness ratio are more important for determining the effective Young's modulus.

Band gap properties

In this part of the article, the dispersion relations of star-shaped honeycombs are laid forth in the form of gap maps and dispersion diagrams. Because of the potential for numerical mistakes at high frequencies, the current study only takes into account the first

10 wave modes. In the computational simulations, the frequency ω_0 is normalised with regard to the initial flexural resonance ω_0 of a simply supported beam (length l , breadth b , and uniform thickness t), namely $\omega_0 = 0$, where: l = length, b = width, and t = thickness uniformly distributed along the beam.

$$\omega_0 = \frac{\pi^2}{l^2} \sqrt{\frac{EI}{\rho A}}$$

With A being expressed by equation (10).

Our strategy is mostly based on the comparative analysis of square lattice structures that is given in. This study is used to test the correctness of the formulations and programmes that we have developed. Figure 10 depicts the band structure of square lattice structures by taking the values $\nu_{12} = 0$, $\nu_{12} = 0.5$, $a = 4$, $l = 3$, 50 and $\theta = 180^\circ$ of the star-shaped honeycombs. This was done in order to determine the square lattice structures' band structures (a). Because the values of ν_{12} are proportional to the results given in the literature due to different normalised definitions of the flexural resonance ω_0 , it is clear that the proposed numerical method is effective and accurate. This is demonstrated by the fact that the evolution of the dispersion curves agrees well with those given in. Furthermore, it can be shown in Figure 10(a) that there are no full band gaps present in the square cellular honeycombs. Figure 10 illustrates the band structure of one example with $\nu_{12} = 1$, 0.1 , 0.1 , $a = 1$ and $\theta = 70^\circ$. This is done in order to demonstrate the benefits that star-shaped honeycombs have on band characteristics (b). It has been discovered that there are three 'stop bands' that exist

between the no dimensional frequencies of = 0.23 0.27, = 0.36 0.49, and = 0.55 1.22. In the context of applications involving mechanical filters and vibration isolation, these low frequency band gaps reveal that starshaped honeycombs are preferable than typical square cellular honeycombs. The following analysis provides an overview of a more in-depth research that investigates how the dependency of the alldirectional band gaps on geometrical factors works. As can be seen in figure 11, we were able to determine shifts in the normalised frequencies of the all-directional band gap borders by adjusting the values of four different independent parameters:., a l, and. In the sake of keeping things simple, every single set of geometrical parameters that are referenced in the numerical examples are exactly the same as those that are presented. In addition, it is important to note that the tiny gaps with widths smaller than 0.02 in the whole range of parameters that were taken into consideration were not taken into account since they were ignored. It is common knowledge that one of the most appealing characteristics of acoustic met materials is the possibility of tailoring the desired band gap to stop the propagation of waves of certain frequencies. This is particularly useful for the construction of low frequency band gaps and is one of the most attractive features of acoustic metamaterials. Among the first 10 frequencies, a comparison of the four sub-figures that make up figure 11

demonstrates rather plainly that the band gaps are mostly concentrated in the frequency ranges of 4th–5th, 6th–7th, and 8th–9th respectively. Each of the band gaps has the potential to be dramatically modified by any one of the four independent factors, which are denoted by the symbols., a l and. It should be noted that certain significant band gaps may be produced by modifying the parameters that are being studied, such as the 6th–7th and 8th–9th ones, as seen in figures 11(a) and 11(b), respectively (b). A total of band gap widths, with or without normalisation relative to the mean frequency, is included [26] in order to further investigate the influence of these four geometrical factors on the band gap features of star-shaped honeycombs.

$$f_1(\Delta\omega_{relative}) = \sum_{i=1}^3 \left[\frac{\omega_u^i - \omega_l^i}{(\omega_u^i + \omega_l^i)/2} \right]$$

$$f_2(\Delta\omega) = \sum_{i=1}^3 (\omega_u^i - \omega_l^i)$$

Where the frequencies u I and l I represent, respectively, the upper edge limit of the ith band gap and the lower edge limit of the ith band gap As can be seen in figure 7 u I and l I correspond to the fourth and fifth frequencies, respectively, for the first band gap that corresponds to the value of 1. The concept being put forth

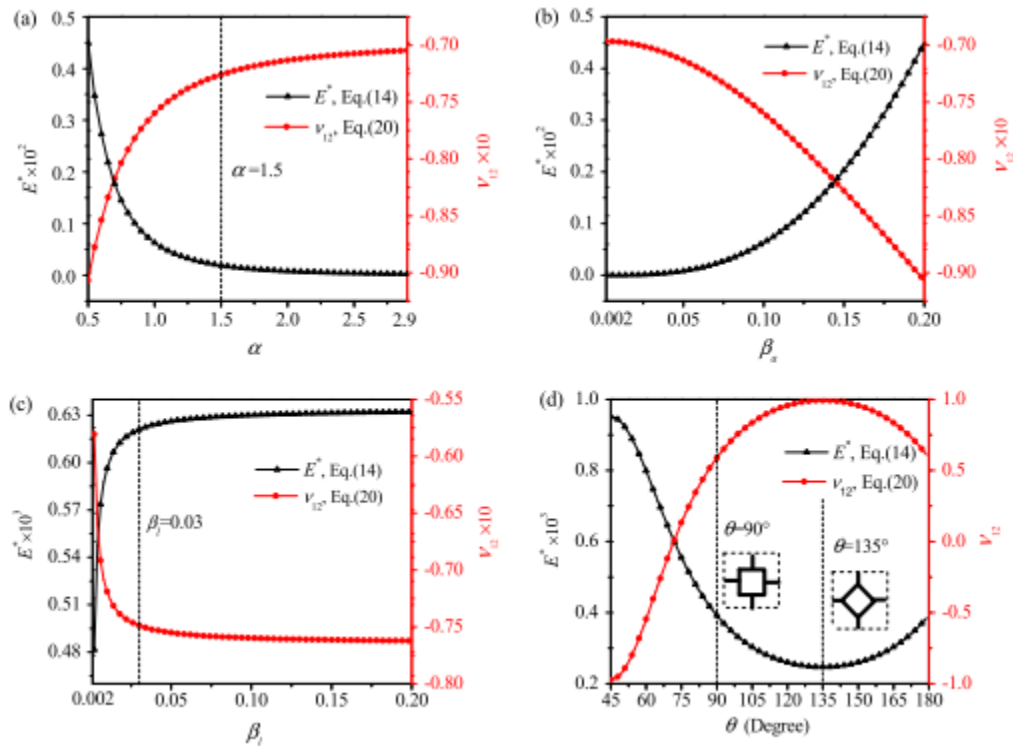


Figure 7: The effective constants of a honeycomb in the shape of a star versus (a) the cell wall aspect ratio with 0.1, 0.1 $l = \dots$ and $\theta = 70^\circ$, (b) the slenderness ratio a with 1, 0.1 $l = \dots$, (c) the slenderness ratio l with 1, 0.1 $a = \dots$, and (d) the internal angles with

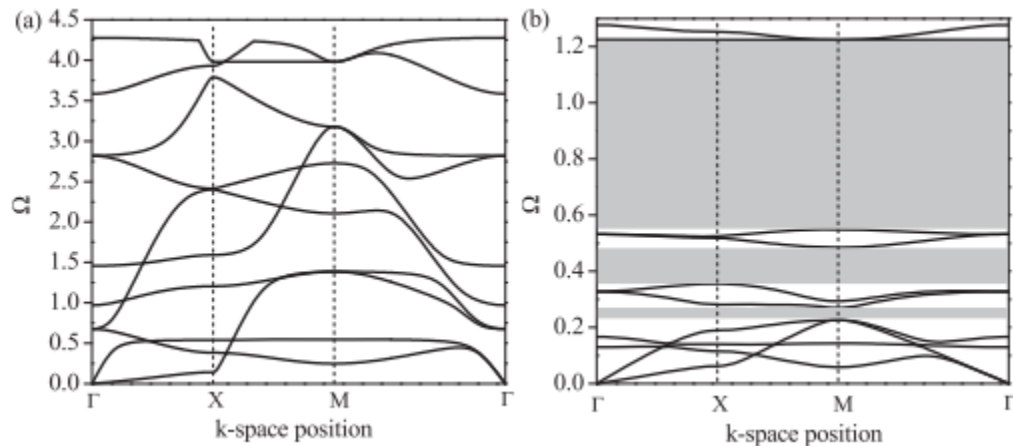


Figure 8. Band structures of (a) square lattice structures by taking 0, 0, 4 3 50 $l = \dots$ and $\theta = 180^\circ$ of star-shaped honeycombs for a comparative study and (b) star-shaped honeycombs with 1, 0.1, 0.1 $l = \dots$ and $\theta = 70^\circ$. a) Band structures of (b) star-shaped honeycombs with 1, 0.1, 0.1 The region that is shaded represents the gaps between the bands.

Conclusions

For the purpose of creating an acoustic superlens in water, we suggest making use of a Metamaterial in the shape of a star. The band structure of the metamaterial, as well as the effective parameter values, provide the impression that it possesses double-negative index qualities in the frequency band ranging from 8760 to 9574 Hz, which is the frequency range in which its refractive indices are negative. Simulations of negative refraction and eigen frequency contours further confirm that the refractive index of the star-shaped structure is about one when it operates at 9380 Hz. This indicates that the lens is able to concentrate sound waves operating at this frequency. According to the results of numerical simulations, the lens has a spatial resolution of 0.39, which is significantly lower than the diffraction limit of 0.5. In this study, we present investigations into the in-plane effective elastic constants and band-gap behaviours of star-shaped honeycombs. These behaviours have been the subject of previous research. When it comes to parameter studies, the findings indicate that when the four independent parameters, a , l and ν are raised, the normalised Young's modulus E^* and Poisson's ratio ν_2 exhibit opposing tendencies. This is the case when the parameters are increased. This suggests that the NPR offers an improved effective Young's modulus of star-shaped honeycomb structures. The findings of parameter studies performed on the features of wave propagation demonstrate that the four factors studied, a , l , ν and ν_2 , can greatly impact band-gap characteristics. In addition, an intriguing phenomena has been seen, which is

that the absolute band width f_2 tends to level off, although the relative band width f_1 slightly increases. This is because the absolute band width f_2 is proportional to the relative band width f_1 . This demonstrates that the value of the sum of band gap widths has remained the same, as was to be predicted, and that the band gap may be configured in low frequencies.

References

1. Pendry, J. B. Negative refraction makes a perfect lens. *Phys. Rev. Lett.* 85(18), 3966–3969 (2000).
2. Zhang, X. & Liu, Z. Superlenses to overcome the diffraction limit. *Nat. Mat.* 7(6), 435 (2008).
3. Liu, F. et al. Parallel acoustic near-field microscope: A steel slab with a periodic array of slits. *Phys. Rev. E* 80, 026603 (2009).
4. Zigoneanu, L., Popa, B. I. & Cummer, S. A. Design and measurements of a broadband two-dimensional acoustic lens. *Phys. Rev. B* 84(2), 024305 (2011).
5. Liu, A., Zhou, X., Huang, G. & Hu, G. Super-resolution imaging by resonant tunneling in anisotropic acoustic metamaterials. *J. Acoust. Soc. Am.* 132(4), 2800–2806 (2012).
6. Fang, N. et al. Ultrasonic metamaterials with negative modulus. *Nat. Mater.* 5(6), 452–456 (2006).
7. Lee, S. H., Park, C. M., Yong, M. S., Wang, Z. G. & Kim, C. K. Acoustic metamaterial with negative modulus. *J. Phys. Condens. Mat.* 21(17), 175704 (2009).

8. Liu, Z. et al. Locally resonant sonic materials. *Science* 289(5485), 1734–1736 (2000).
9. Yang, Z., Mei, J., Yang, M., Chan, N. H. & Sheng, P. Membrane-type acoustic metamaterial with negative dynamic mass. *Phys. Rev. Lett.* 101(20), 204301 (2008).
10. Lu T, Zhang Q and Jin F 2012 Recent progress in the development of lightweight porous materials and structures *Mater. China* 31 13–25
11. Spadoni A, Ruzzene M, Gonella S and Scarpa F 2009 Phononic properties of hexagonal chiral lattices *Wave Motion* 46 435–50
12. Prawoto Y 2012 Seeing auxetic materials from the mechanics point of view: a structural review on the negative Poisson's ratio *Comput. Mater. Sci.* 58 140–53
13. Liu Y and Hu H 2010 A review on auxetic structures and polymeric materials *Sci. Res. Essays* 5 1052–63
14. Yang D U, Lee S and Huang F Y 2003 Geometric effects on micropolar elastic honeycomb structure with negative Poisson's ratio using the finite element method *Finite Elem. Anal. Des.* 39 187–205
15. Tomlinson G, Panayiotou P and Scarpa F 2000 Numerical and experimental uniaxial loading on in-plane auxetic honeycombs *J. Strain Anal. Eng. Des.* 35 383–8